



Temperature-driven mechanisms of hydrogen embrittlement and electrochemical corrosion in Ni-based superalloy 600

Jiaqing Li ^a, Xi Yu ^a, Zhiye Zheng ^a, Kai Lu ^{a,*} , Lin Teng ^a, Yu Ding ^b, Zhuwu Zhang ^a, Hui Wang ^c, Che Zhang ^{d,**} , Lilong Jiang ^e

^a College of Chemical Engineering, Fuzhou University, Fuzhou, 350116, China

^b Department of Structural Engineering, Norwegian University of Science and Technology (NTNU), Trondheim, 7491, Norway

^c Institute for Industrial Science, The University of Tokyo, Chiba, 153-8505, Japan

^d Department of Mechanical Engineering, The University of Melbourne, Parkville, VIC, 3010, Australia

^e National Engineering Research Centre of Chemical Fertilizer Catalyst, Fuzhou University, Fuzhou, 350002, China



ARTICLE INFO

Keywords:

Intergranular corrosion
Temperature threshold
Hydrogen-induced brittle fracture
Hydrogen-dislocation-grain boundary interaction
Ni-based superalloy

ABSTRACT

The temperature-dependent mechanisms for hydrogen-induced embrittlement and electrochemical corrosion in Ni-based superalloy 600 have been unravelled by means of tensile tests and potentiodynamic polarization tests under electrochemical environment. Increasing temperature accelerates electrochemical corrosion behaviour and induces the transition into intergranular corrosion, whereas there exists critical temperature $T_{HE, max}$, in which hydrogen-induced ductility loss reaches its peak. Detailed electron microscopy and thermal desorption spectroscopy analysis demystify that intergranular brittle fracture at $T_{HE, max}$ is predominantly driven by hydrogen-dislocation-grain boundary interactions, compounded by high diffusible hydrogen content. These findings offer new insights into the critical role of temperature in modulating hydrogen embrittlement and corrosion, contributing to the design of materials in hydrogen environment.

1. Introduction

Hydrogen, as a versatile clean energy carrier and storage medium, is addressing the intermittency challenge of renewable sources and revolutionizing a number of industrial processes [1–4]. Ni-based superalloys, i.e., commercial Alloy 600, have a variety of hydrogen-related industrial applications such as hydrogen gas turbine components, pressurized water reactors, and others, due to their superior mechanical properties and damage tolerance [5–8]. However, a longstanding exposure to a hydrogen environment can induce severe degradation in mechanical performance [9,10] such as a loss in ductility [11–16], and a sudden brittle rupture [17–20], which is known as hydrogen embrittlement (HE).

Heretofore, some studies have been reported to shed light on the long-term uncertainties in regard to HE mechanisms of Ni-based superalloys [15,16,21–23]. Michler et al. [21] investigated HE effects on austenitic Fe–Cr–Ni alloys like 316 L stainless steel, Incoloy DS, Incoloy 925, Inconel 600, and Chromel A in a gaseous hydrogen atmosphere. They proposed that HE of ternary Fe–Cr–Ni alloys was contingent upon

respective microstructural features. Specifically, alloys with a pure austenitic microstructure showed no hydrogen-induced degradation in tensile ductility, whereas microstructures with carbide precipitates on the grain boundaries (GBs) exhibited intergranular fracture associated with GB decohesion. On the other hand, hydrogen concentration and strain rate can also alter the hydrogen-induced failure model of Ni-based superalloys. For instance, Murakami et al. [22] inferred that fracture strain in Inconel alloy decreased as hydrogen content charged by electrolysis increased, and high hydrogen contents changed the fracture of alloy from a quasi-cleavage transgranular brittle fracture to a predominantly intergranular brittle fracture. Lecoester et al. [23] flagged up that the fracture mode of Inconel 600 may change from fully brittle intergranular at low strain rate to fully ductile at high strain rate with a mixed mode in an intermediate range of strain rate.

The HE behaviour is not only governed by the aforementioned microstructural features, hydrogen concentration, and strain rate, but also determined by temperature [24]. Some authors have explored the role of temperature in HE in Ni-based superalloys and particularly the contribution of temperature to hydrogen transport by dislocations in the

* Corresponding author.

** Corresponding author.

E-mail addresses: lu.kai@fzu.edu.cn (K. Lu), che.zhang@unimelb.edu.au (C. Zhang).

embrittlement process [23,25–27]. Lecoester et al. [23] reported the HE characteristics of Alloy 600 at a temperature range from 293K to 673K, revealing that the HE sensitivity decreased at high temperature. This observation was presumably due to a reduction in the amount of hydrogen trapped and transported by mobile dislocations when the testing temperature increased. Chène et al. [27] further invoked that the HE of Alloy 600 fully disappeared at very low temperature below 180K. Such phenomenon can be attributed to low hydrogen diffusion and weak hydrogen interaction with dislocations at cryogenic temperature. However, others have shown a seemingly contradicting result. For instance, Noguchi et al. [28] pointed out that the loss of ductility for Ni-based superalloys under a pressurized hydrogen environment at 200 °C–300 °C was somewhat comparable to that at 25 °C. Such contradiction is likely due to the discrepancy in the test conditions, such as hydrogen content (hydrogen charging method), or moving dislocations (strain rate). In the Noguchi's experiments, the hydrogen concentration was ≈5500–5800 ppm so that the detrimental effect of hydrogen was still obvious even at high temperature. As a consequence, these hitherto-known arguments increase the complexity in elucidating the temperature dependence and determining the temperature threshold of HE of Ni-based superalloy 600. Note that the majority of prior research has focused on studying the temperature-dependent HE under pre-charging conditions. While this method enables controlling the pre-charging temperature to minimize the time required to attain a consistent hydrogen concentration across the sample, the results can be affected by hydrogen loss, depending on the mechanical testing time and the material diffusivity. Therefore, in order to mimic in-service conditions, it is very essential to further investigate the effect of temperature on the HE of Ni-based superalloy 600 under in-situ hydrogen charging environment. Furthermore, the previous literature about the HE of Ni-based superalloys has been conducted with a rather high tensile strain rate on the order of 10^{-5} – 10^{-3} [29–31]. As the HE is contingent upon loading strain rate, the temperature-dependent HE mechanisms of Ni-based superalloys at a lower tensile strain rate, i.e., 10^{-6} , remain unclear and require further in-depth exploration.

Besides suffering from HE, corrosion problems of Ni-based superalloys can still be observed with their use in highly aggressive environment [29–32]. Heretofore, there have been several studies covering pitting corrosion [33,34], intergranular corrosion [35], and stress corrosion [36,37] of Ni-based superalloys. As a typical influencing factor, temperature has a prominent effect on the corrosion process. Lu et al. [38] reported that at low temperature, the passivation effect of Ni-based single crystal weakened, and discrepancy in self-corrosion potential between phases decreased, rendering smaller variations in corrosion. Lv et al. [39] found that with the increasing temperature, the electrochemical parameters such as self-corrosion potential and passive current density of Ni-based superalloy CMSX-4 shifted in the negative direction, indicating a worse corrosion performance. Increasing temperature not only accelerates the molecular thermal motion, increases the electrolyte dissolution and convective mass transfer, and results in the decrease of solution impedance, but also changes the composition of the corrosion product layer and leads to more holes, cracks, and other defects. Sun et al. [40] found that as the temperature increased, the protective property of the barrier film degraded, leading to the decreased corrosion resistance of the oxide film on Alloy 625. However, there has been little study on the effect of temperature on the corrosion behaviour of Ni-based superalloy 600. Electrochemical corrosion characteristics of Ni-based superalloy 600 at a series of temperatures have never been investigated either.

Considering the aforementioned research gaps, the present study aims to achieve an in-depth understanding of the temperature-dependent behaviour of two distinct phenomena—HE and electrochemical corrosion in Ni-based superalloy 600. Specifically, the study independently investigates (i) the influence of temperature on HE behaviour under in-situ hydrogen charging condition and at a lower tensile strain rate, i.e., 10^{-6} , and (ii) the role of temperature in

electrochemical corrosion characteristics. On the one hand, based on thorough investigations of the obtained electrochemical corrosion response and corrosion morphology, the linkage between corrosion behaviour and temperature was established and analysed. On the other hand, in-situ slow strain rate tensile (SSRT) tests, coupled with multiple electron microscopy techniques, were conducted to determine the temperature threshold of HE. The underlying mechanisms behind the temperature threshold were demystified from the perspectives of hydrogen content and hydrogen-induced intergranular fracture associated with the dynamic hydrogen-dislocation-GB interactions. These findings are beneficial to deepening our understanding of temperature-dependent HE behaviour and the electrochemical corrosion characteristics in Ni-based superalloys. In particular, the demonstration of the temperature threshold of HE would be pivotal to determining the appropriate operating temperature of commercially-available Ni-based superalloys for hydrogen-related practical applications.

2. Experimental details

2.1. Material and microstructural characterization

The Ni-based superalloy 600 used in this study was vacuum-melted and delivered in a solution-annealed condition, whose chemical composition determined by using energy-dispersive X-ray spectroscopy (EDS) is presented in Table 1. The microstructure was characterized by using a Leica DMI8 optical microscope (OM) and a Helios G4 CX scanning electron microscope (SEM) with electron backscattered diffraction (EBSD). For the convenience of measurements, the specimens were chemo-mechanically polished in a colloidal silica suspension to obtain a high surface quality. The grain morphology, which was mapped out by EBSD and analysed by the OIM software, indicates an average grain diameter of about 108.6 μm (Fig. 1(a)) and randomised crystallographic texture with a Σ3 twin boundary of 63.4% (Fig. 1(b)). The EBSD phase map in Fig. 1(c) and OM image in Fig. 1(d) highlight that the microstructure consists of the typical single phase austenite, accompanied by some carbonitrides distributed across the grains. The EDS spectrum in Fig. 1(e) shows that these carbonitrides are $Ti(C_xN_y)$ with a higher Ti, C and N content than the matrix.

2.2. Hydrogen charging and slow strain rate tensile tests

Tensile specimens with a gauge dimension of 30 mm × 6 mm × 1.4 mm were machined by electrical discharge machining (EDM). All the specimens were ground from #180 up to #2000 by a series of SiC papers to a final thickness of 1.0 mm. The gauge parts of the specimens were electrochemically pre-charged with a constant current density of 50 mA/cm² for 24 h in 0.1 mol/L H₂SO₄ solution with 5 g L⁻¹ CH₄N₂S [12, 41,42]. Given the hydrogen diffusion coefficient of 7.003×10^{-13} m²/s determined by electrochemical hydrogen permeation tests, the hydrogen pre-charging process and in-situ hydrogen charging can facilitate hydrogen diffusion and ensure a homogeneous distribution of hydrogen atoms throughout the specimens. The SSRT tests were carried out with an initial strain rate of 10^{-6} s⁻¹ using a SHIMADZU tensile tester. Throughout the entire tensile loading phase, the pre-charged specimens were immersed in the inner chamber of electrochemical cell with the identical electrolyte as the pre-charging condition, and in-situ hydrogen charging method was used to continuously introduce hydrogen into the gauge parts of the specimens at a current density of 50 mA/cm². Meanwhile, the temperature of electrolyte was controlled by means of a constantly circulated thermostatic liquid in the outer chamber of electrochemical cell. The range of temperature was selected from 280K to 330K at an interval of 10K to unravel the effect of temperature on the HE of Ni-based superalloy 600. For comparison, reference tests were carried out at 300 K without hydrogen charging [41,43]. Following the tensile loading, fracture surfaces and neighbouring lateral surfaces of the specimens were characterized by SEM and EBSD.

Table 1

Chemical composition of Ni-based superalloy 600 used in this study (wt.%).

Element	Ni	Cr	Fe	C	Mn	Cu	Co	Ti	Si	Al	N	O	P	S
Wt. (%)	71.78	17.16	7.63	0.06	0.83	0.20	0.33	0.48	0.14	0.10	0.33	0.81	0.06	0.09

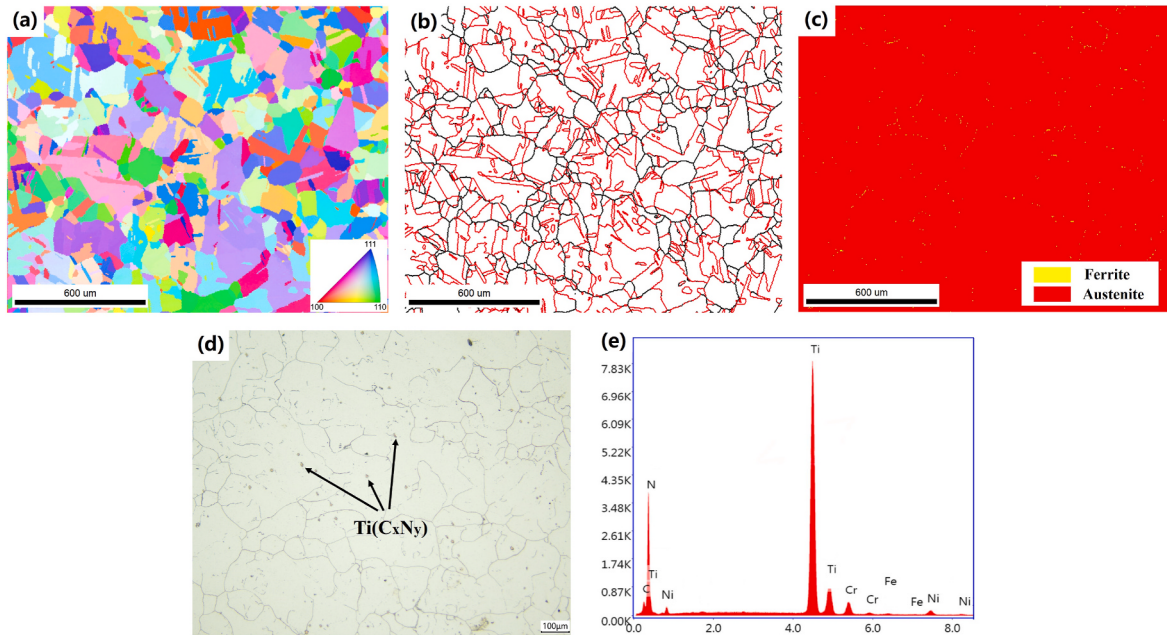


Fig. 1. The microstructure of Ni-based superalloy 600: (a) and (b) Inverse Pole Figure (IPF) and the corresponding GB map, where red lines and black lines indicate the Σ_3 twin boundaries and general boundaries, respectively, (c) EBSD phase map corresponding to the IPF map, (d) OM observation of the morphology of matrix and carbonitrides, and (e) EDS spectrum of the carbonitrides.

2.3. Electrochemical corrosion measurements

The electrochemical corrosion experiments were carried out in 0.1 mol/L H_2SO_4 solution by means of CH Instrument-potentiostat (model CHI604E) with a three-electrode cell system. The specimen of Ni-based superalloy 600 acted as the working electrode, while the Ag/AgCl and Pt-wire served as the reference and counter electrodes, respectively. After each specimen was placed in the working electrolyte, the open-circuit potential (OCP) of the specimen in the solution was measured for 4 h until reaching a stable value (the change of potential less than 0.02 V over 10 min). Subsequently, potentiodynamic polarization curves were initiated from the cathodic potential to the anodic potential with a sweep rate of 1 mV/s. After all electrochemical experiments had been performed, the corrosion morphology of specimens was examined using SEM.

3. Results

3.1. The mechanical property of hydrogen-charged Ni-based superalloy 600 with temperature

Fig. 2 shows the tensile stress-strain curves of specimens with hydrogen charging over a temperature range from 280 K to 330 K. As a reference, the mechanical response of the non-charged material at a temperature of 300 K was also provided [41,43]. These data were obtained from three tensile tests performed on each experimental condition. The Ni-based superalloy 600 devoid of hydrogen shows an ultimate tensile strength of 583 ± 6 MPa and a total elongation of $55.7 \pm 1.2\%$, attributed to the massive solid solution and high strain hardening [44, 45]. At the same temperature (300K), it can be seen that the hydrogen charging case shows no appreciable effect on the elastic modulus and

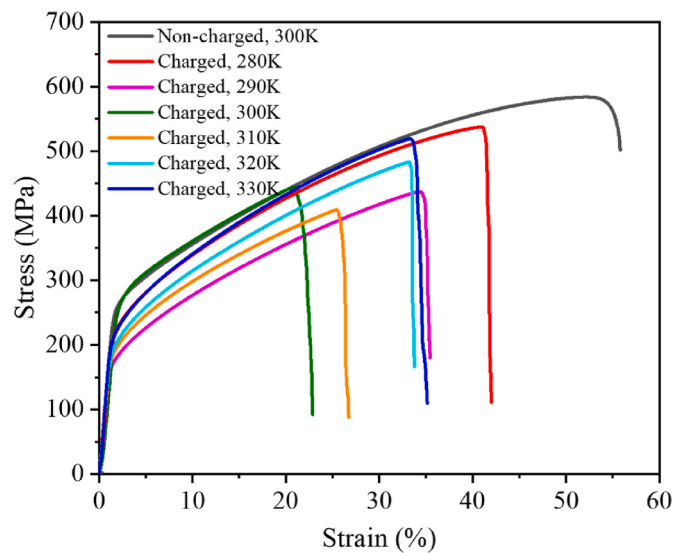


Fig. 2. Stress-strain curves of Ni-based superalloy 600 with hydrogen charging at various temperatures.

yield strength. However, the tensile strength and the total elongation are prominently decreased to 443 ± 3 MPa and $22.8 \pm 1.0\%$, respectively. Further, with respect to the other hydrogen charging temperatures, hydrogen-induced loss in both tensile strength and ductility is also evident from the measured stress-strain curves. Such deleterious effect of hydrogen on the mechanical properties of Ni-based superalloys has been well documented in the past articles [11,13,46].

To further pinpoint the temperature-dependent HE susceptibility of specimens, several representative parameters such as ultimate tensile strength, elongation to failure, reduction in area, and HE index were calculated, and their evolution with the hydrogen charging temperature is depicted in Fig. 3. The reduction in area can be expressed as where and are the original cross-sectional area of a specimen and the area of its smallest cross section after testing, and HE index can be defined as where and are the reduction in area of non-charged and hydrogen-charged specimens, respectively. Fig. 3 clearly exhibits that the values of ultimate tensile strength, elongation to failure and reduction in area of hydrogen-charged specimens are lower than those of non-charged cases. Moreover, the degradation in ductility due to hydrogen charging is seemingly contingent upon the temperature. Specifically, the elongation to failure and reduction in area of hydrogen-charged specimens initially decrease from $42.0 \pm 1.6\%$ and $35.4 \pm 1.3\%$ to $22.8 \pm 1.0\%$ and $17.3 \pm 1.2\%$ as the temperature shifts from 280K to 300K, while showing an upward tendency when the temperature exceeds 300K up to 330K. Herein, both parameters exhibit their minima at a temperature of 300K, in other words, hydrogen-induced degradation reaches its maximum. The higher HE index generally suggests more severe HE susceptibility. The HE index versus temperature in Fig. 3(d) again shows that the value of 300K is the temperature threshold of $T_{HE, max}$, where the

HE susceptibility is the highest, i.e., $62.9 \pm 2.3\%$, and the embrittlement effect is less above and below this temperature. The observation of $T_{HE, max}$ occurring at Ni-based superalloy 600 can be compatible to the experimental data obtained from other structural materials in the previous literature [42,47–49].

3.2. The fracture morphology of hydrogen-charged Ni-based superalloy 600 with temperature

Considering the importance of ductile-to-brittle transition in the fracture mode for understanding hydrogen-induced embrittlement mechanism, detailed post-mortem fractographic characterization was carried out in Ni-based superalloy 600 without and with hydrogen charging at various temperatures. In the case of the non-charged specimens, the fracture morphology indicates a ductile pattern, with numerous voids and dimples being observed throughout the fracture surface, as seen in Fig. 4(a₁)–4(a₃). In contrast, at a hydrogen charging temperature of 290K, a preponderant proportion of dimples and some quasi-cleavage features are manifested around the fracture surfaces of the hydrogen-charged specimens, as shown in Fig. 5(a₁)–5(a₃). The emergence of quasi-cleavage fracture is an evident support of HE effect, but this effect is tangential or secondary to the failure process since the

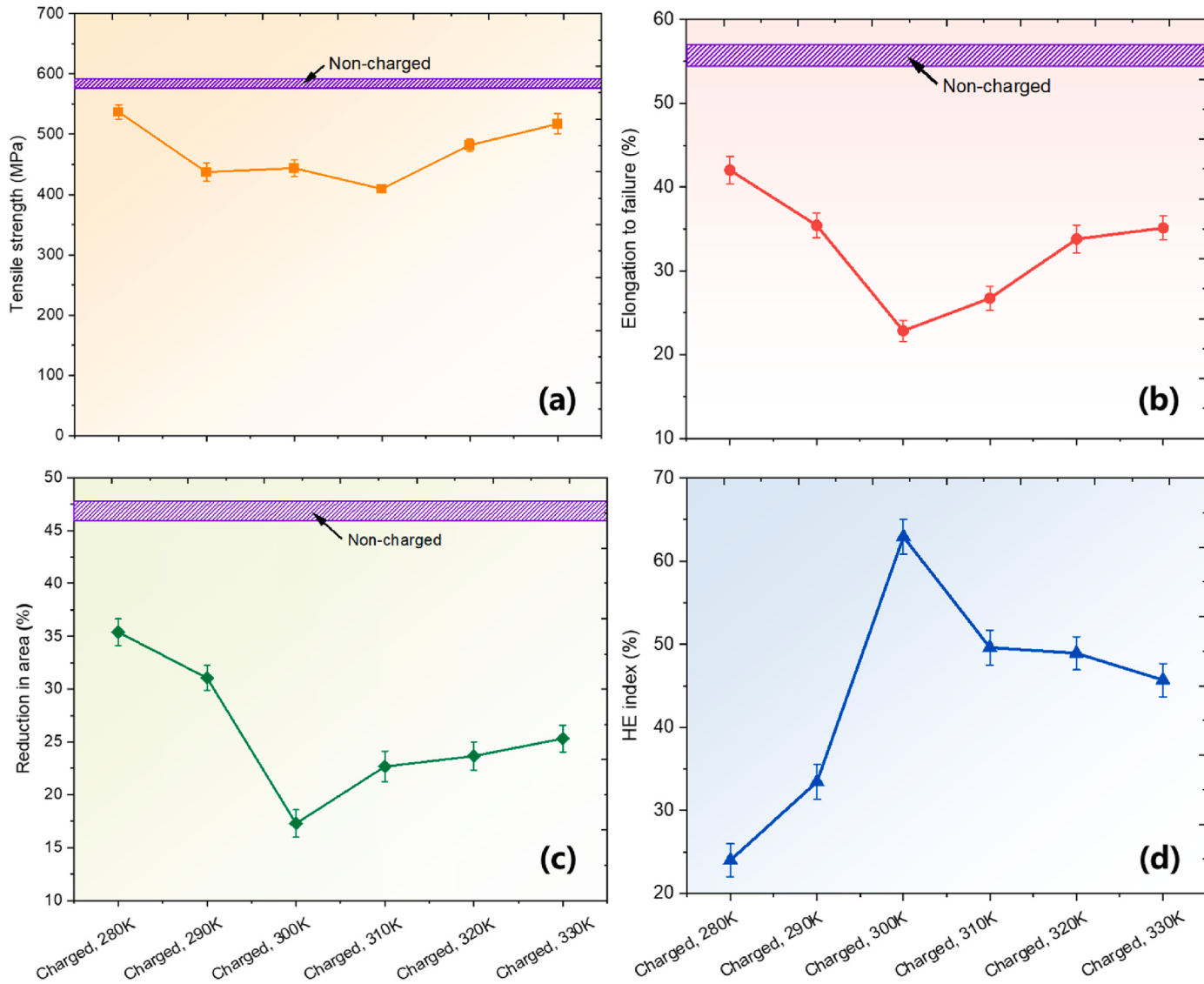


Fig. 3. The dependence of mechanical property parameters on experimental conditions.

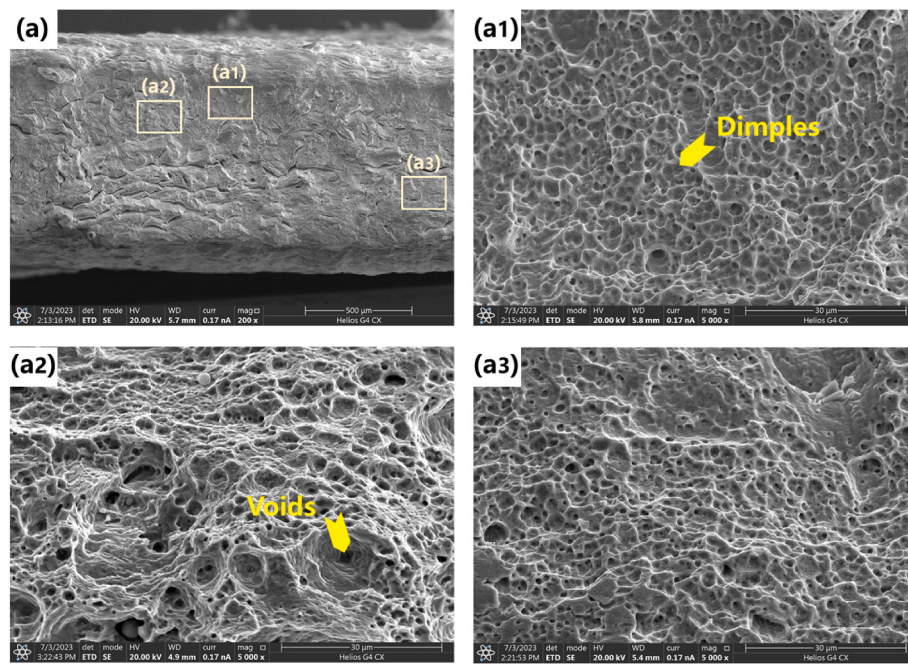


Fig. 4. Microscale SEM images of the fracture surfaces of non-charged specimens after the SSRT tests.

overall fracture mode remains ductile.

Compared to the case of 290K, the hydrogen charging at 300K prominently alters the fracture morphology from ductile rupture to brittle-like flat-faceted rupture, as shown in Fig. 5(b). The SEM images in Fig. 5(b1)-5(b3) indicate that the facets manifest with intergranular brittle fracture and secondary cracks. These brittle features have also been invoked in previous literature on the HE of Ni-based superalloys under tensile loading [13,19,20,50]. For instance, after studying fracture mechanism of hydrogen-charged Fe-Ni-Cr based superalloy A286, Takakuwa et al. [13] unveiled that the fracture surface was covered with a large number of facets, being suggestive of intergranular brittle-like fracture. As the temperature further increases, i.e., at a temperature of 320K, a prevalent ductile failure mode characterised by plenty of dimples and voids can be once again observed as displayed in Fig. 5(c).

On the basis of the above fractographic analysis, it can be deduced that the ductility declines prominently as the temperature shifts to 300 K, and then increases with further temperature. At the temperature threshold $T_{HE, max}$ of 300K, brittle-like facets like intergranular fracture emerge, inferring that HE susceptibility is the highest and in concordance with the HE index in Fig. 3.

3.3. Electrochemical corrosion behaviour of Ni-based superalloy 600

Fig. 6 displays the evolution of the OCP of Ni-based superalloy 600 as a function of temperature in 0.1 mol/L H₂SO₄ solution. It can be seen that the OCP of Ni-based superalloy 600 in H₂SO₄ solution initially experiences fluctuation and eventually reaches quasi-steady-state value after 4 h exposure. It is generally accepted that a lower OCP value indicates a higher electrochemical activity and greater active corrosion tendency. Upon increasing the temperature, the final OCP value shifts in the negative direction, suggesting that temperature is an activating factor in electrochemical corrosion. Potentiodynamic polarization experiments with different temperatures were performed, with the results compiled in Fig. 7. As depicted, there exists a discernible passivation region at the range of 0–1 V, in which a stable barrier film can be formed. Note that with the final potential exceeding any potentials in the passivation region, the current density rapidly increases, manifesting the occurrence of localised corrosion of Ni-based superalloy 600 under a high potential [51–53].

Fig. 8 demonstrates the corrosion morphology of Ni-based superalloy 600 after potentiodynamic polarization tests at various temperatures. At a temperature of 290K, the surface of the Ni-based superalloy presents no notable corrosion feature. The higher magnification image in Fig. 8(a1) indicates a few corrosion pits. However, with increasing the temperature, i.e., at 310K in Fig. 8(b), obvious signs of pitting corrosion can be observed, evidenced by larger corrosion area and more corrosion pits. As the temperature further shifts to 330K, the Ni-based superalloy exhibits larger corrosion pits within the grains and intergranular corrosion in Fig. 8(c). The coarsening and augment of corrosion pits as well as the appearance of intergranular corrosion [54,55] indicate the exacerbation of corrosion process due to temperature, which can be linked with electrochemical corrosion results depicted in Figs. 6 and 7.

4. Discussion

The temperature dependence of HE and electrochemical corrosion in Ni-based superalloys was systematically investigated in the present study. Throughout the test temperature range of 280K–330 K, the corrosion susceptibility of Ni-based superalloy 600 in 0.1 mol/L H₂SO₄ solution is increased with the increase of temperature. This can be ascribed to the fact that with increasing the temperature the electrolyte dissolution increases and convective mass transfer becomes easier, resulting in the decrease of solution impedance [56–58]. As a consequence, at elevated temperature the barrier film in the passivation region is more porous and less protective, thus leading to more severe corrosion, i.e., the intergranular corrosion at 330K. In contrast, HE susceptibility of Ni-based superalloy 600 in 0.1 mol/L H₂SO₄ solution is found to exhibit a rather complicated relationship with the test temperature range of 280K–330K. The embrittling effect is exacerbated as the temperature increases up to 300K, but alleviated at higher temperature, which suggests a temperature threshold $T_{HE, max}$ of 300K with the maximum HE susceptibility. In the following, we comprehensively demystify the underlying mechanisms behind $T_{HE, max}$ from the perspectives of hydrogen content and hydrogen-induced intergranular cracking associated with hydrogen-dislocation-GB interactions.

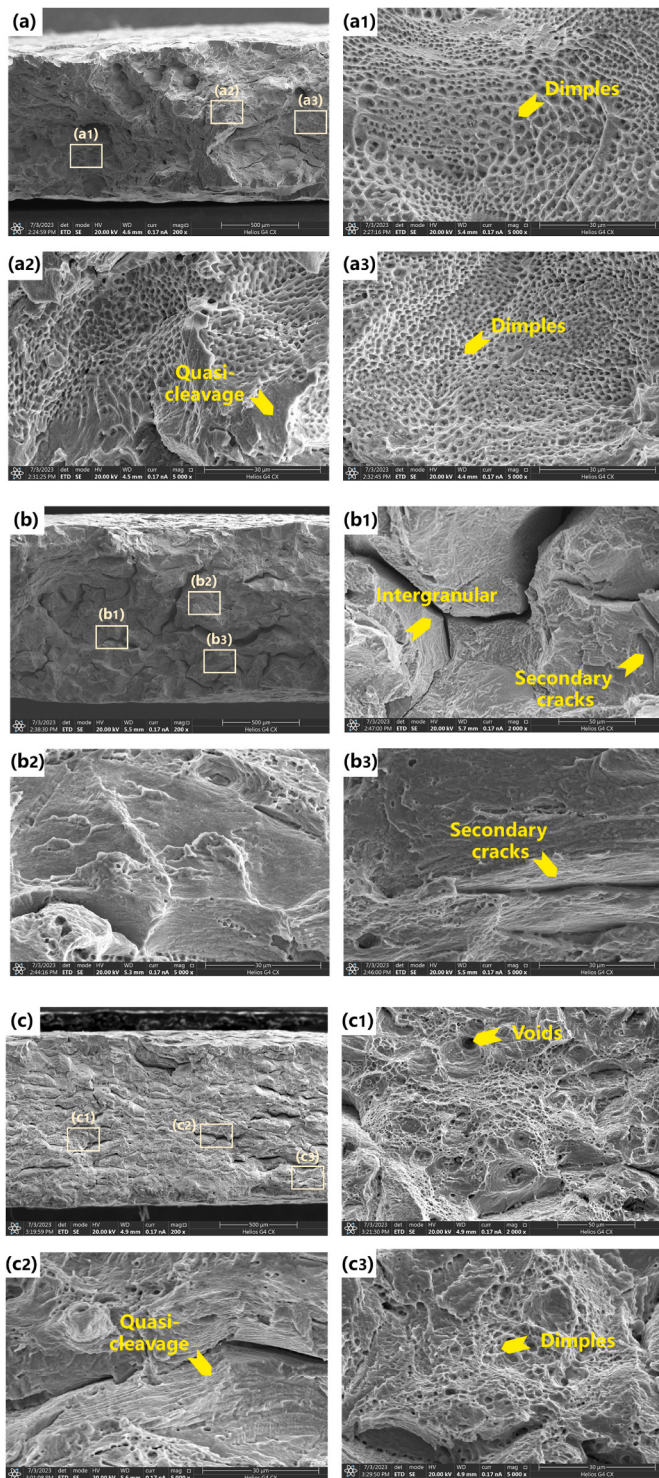


Fig. 5. Microscale SEM images of the fracture surfaces of hydrogen-charged specimens after the SSRT tests at various temperatures (a) 290K, (b) 300K, and (c) 320K.

4.1. Hydrogen quantification tests

The total hydrogen content in the specimens at hydrogen charging temperature of 290K, 300K and 320K was measured by thermal desorption spectroscopy (TDS), with the results shown in Fig. 9(a). The TDS experiments were performed with separately prepared specimens. Specifically, the specimens were first electrochemically charged, and then placed into a heating furnace. The heating furnace was heated at a

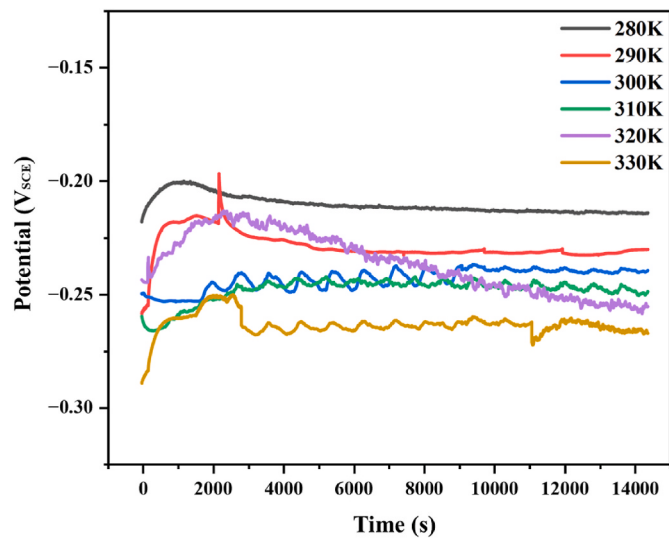


Fig. 6. The OCP of Ni-based superalloy 600 in 0.1 mol/L H₂SO₄ solution at various temperatures.

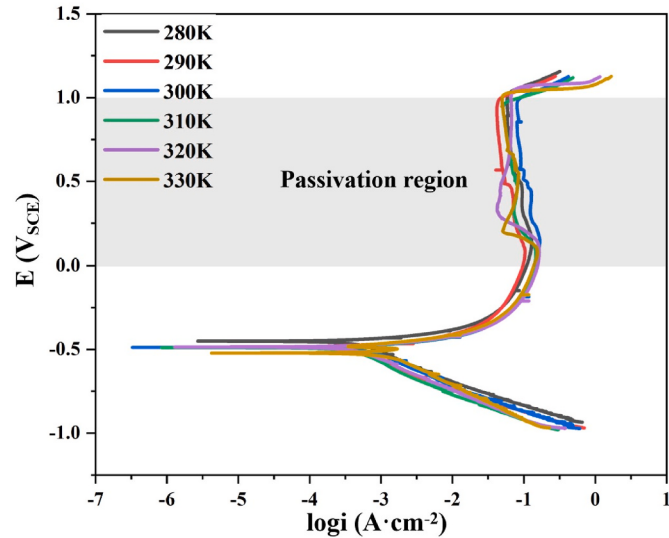


Fig. 7. Potentiodynamic polarization curves of Ni-based superalloy 600 in 0.1 mol/L H₂SO₄ solution at various temperatures.

100 °C/h rate from 25 °C to 600 °C in the Ar atmosphere, and the cumulative desorbed hydrogen was finally measured by using a gas chromatography system. For all hydrogen charging temperature, each hydrogen desorption rate curve can be regarded as the accumulation of two main curves from 100 °C to 600 °C. The total hydrogen content in Ni-based superalloy specimens is found to be contingent upon hydrogen charging temperature. The value at a hydrogen charging temperature of 300K is 18.6 wt ppm, which becomes less when the temperature is above or below 300K, i.e., 4.4 wt ppm at 290K, and 6.6 wt ppm at 320K. This observation can be explained in terms of the hydrogen evolution reaction. The specimens in the present study were electrochemically hydrogen-charged at a constant current density of 50 mA/cm². Hydrogen adsorption and desorption on the surface of specimens can be illuminated by a multi-step electrochemical process as follows [59–62]:



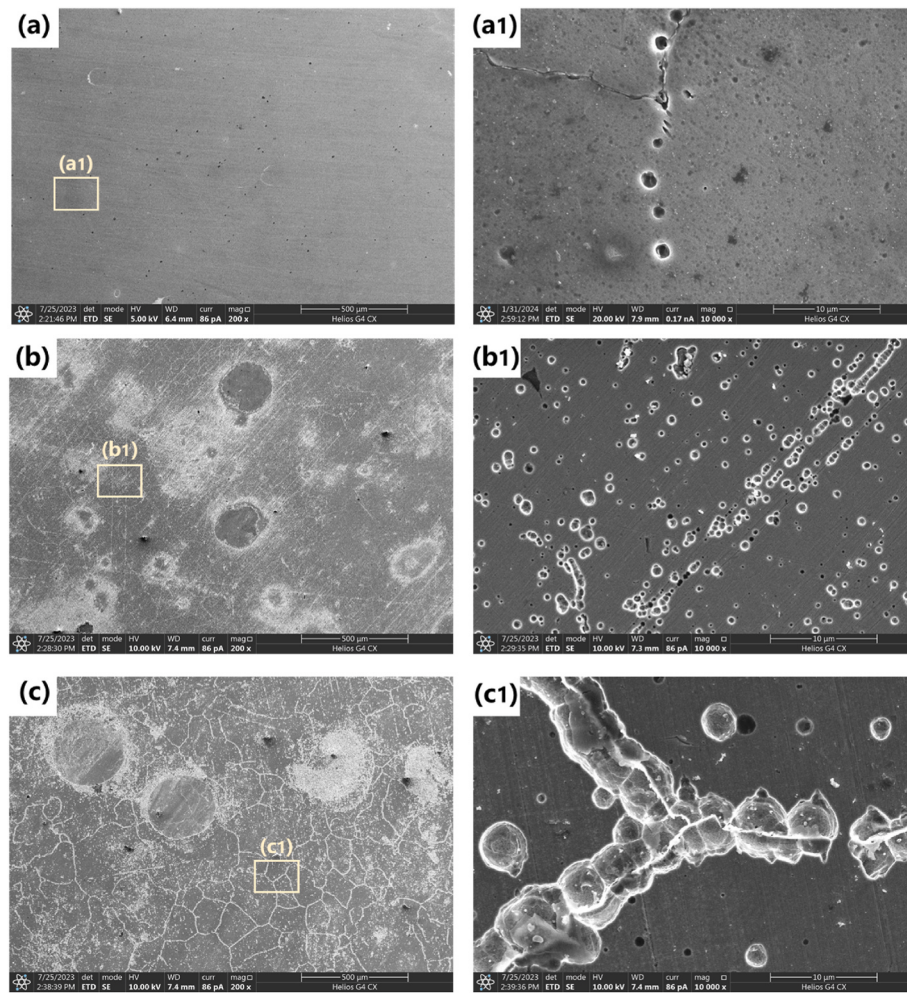


Fig. 8. The corrosion morphology of Ni-based superalloy 600 after potentiodynamic polarization tests in 0.1 mol/L H₂SO₄ solution at various temperature: (a) 290 K, (b) 310 K, and (c) 330 K. (a1)–(c1) are enlarged images marked in (a), (b) and (c), respectively.



Herein the “ H_{ads} ” refers to the adsorbed hydrogen atoms. The Volmer step involves an initial discharge of the hydrogen ion and the generation of adsorbed hydrogen atoms (hydrogen adsorption), while the Heyrovsky and/or the Tafel reaction dominate the subsequent formation of H₂ (hydrogen desorption). It has been inferred that at higher temperature the increase of hydrogen ion activity promotes the Volmer reaction, and thus encourages hydrogen adsorption [63]. On the other hand, elevated temperature can facilitate hydrogen desorption through considerably reduced Tafel slopes and electrochemical energies of activation [64,65]. As such, with increasing the temperature hydrogen adsorption reaction competes with hydrogen desorption process, ultimately determining the hydrogen concentration on the surface of specimens. Such competition can render the highest hydrogen concentration on the surface of specimens at a critical temperature [66]. Obviously, the present study reveals the temperature threshold $T_{HE, max}$ of Ni-based superalloy 600 is 300K. At the hydrogen charging temperature of 300K, hydrogen concentration on the surface of specimens reaches its maximum, which encourages more hydrogen atoms to enter into the interior of specimens and thus produces the highest total hydrogen content in the specimens.

Fig. 9 shows two distinct hydrogen desorption peaks for each desorption rate curve. Gaussian function with a coefficient of determination higher than 0.99 was applied to decompose these two peaks into two main curves (curve 1 and 2) as shown in Fig. 9(b)–(d). The desorption peaks of curves 1 and 2 are located at 140–160 °C and

280–300 °C, respectively. According to the previous study [67], these peaks correspond to hydrogen diffusion processes. Specifically, the desorption peak of curve 1 represents hydrogen diffusion towards the surface, while the desorption peak of curve 2 indicates the back diffusion process, in which hydrogen migrates first to the centre and then to the opposite surface of the specimens. The lower-temperature desorption peak of curve 1 refers to reversible hydrogen traps, such as dislocations and GBs. Meanwhile, the desorption peak of curve 2 is likely associated with dislocations or austenite lattices [68].

The content of diffusible hydrogen in curve 1 and curve 2 is calculated and tabulated in Table 2. Worthy to note here is that a large amount of Σ3 twin boundary shown in Fig. 1(b) is not considered to trap diffusible hydrogen in curve 1 because the Σ3 twin boundary in Ni was found to have a negligibly low hydrogen segregation energy of -0.04 eV [69,70], compared to Ni GBs of -0.16 eV ~ -0.28 eV [69], and dislocations of approximately -0.1 eV [71]. Similar to the total hydrogen content, diffusible hydrogen content in curve 1 and curve 2 also reaches its maximum at a hydrogen charging temperature of 300K. This can be directly linked to the observation of the highest HE susceptibility and intergranular brittle-like fracture at $T_{HE, max}$ in Figs. 3 and 5.

4.2. Hydrogen-induced failure mechanism behind $T_{HE, max}$

To unravel the underlying mechanisms behind $T_{HE, max}$, additional fractographic and crystallographic analysis using SEM and EBSD was carried out in the hydrogen-charged Ni-based superalloy 600. Fig. 10

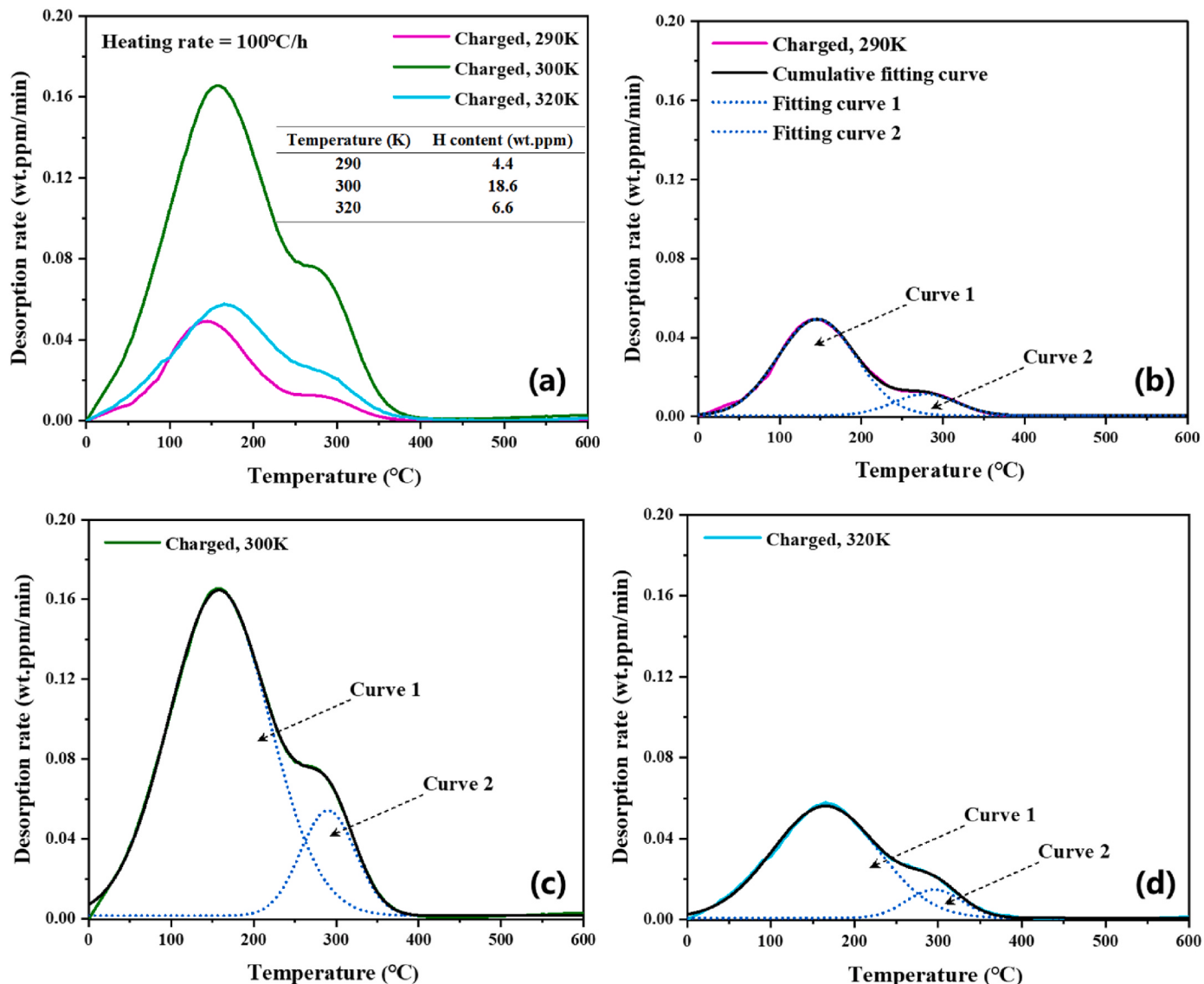


Fig. 9. Analysis of hydrogen content. (a) TDS curves for Ni-based superalloy specimens charged at 290 K, 300 K and 320 K. According to the Gaussian function, peak fitting was conducted separately for the hydrogen desorption curves of hydrogen-charged specimens at (b) 290 K, (c) 300 K and (d) 320 K. Each experimental curve was fitted with a sum of two Gaussian curves (curve 1 and 2).

Table 2

The measured hydrogen content of the specimens by TDS. Each TDS measurement was repeated three times. The averaged value of hydrogen content and the standard deviation of the values are given in the table accordingly.

Hydrogen charging temperature	290K	300K	320K
Total hydrogen (wt. ppm)	4.4 ± 0.04	18.6 ± 0.09	6.6 ± 0.07
Curve 1	3.7 ± 0.02	15.9 ± 0.05	5.8 ± 0.04
Curve 2	0.7 ± 0.02	2.7 ± 0.04	0.8 ± 0.03

shows high magnified SEM images of brittle-like intergranular fracture surface at a hydrogen charging temperature of 300K. It can be clear from Fig. 10(a) and (c) that numerous saw-teeth features exist regularly along the striped bands, like “tear troughs”. Although the intergranular fracture of the marked area in Fig. 10(b) appears to be flat, there are also extensive tiny dimples on the GBs according to the high-magnification view in Fig. 10(d). Therefore, it is reasonable to infer that brittle-like fracture at $T_{HE, max}$ is not a result of pure hydrogen-enhanced decohesion (HEDE) but involves extensive dislocation plasticity adjacent to the GBs induced by hydrogen.

Figs. 11,12,14 show the crystal orientation and corresponding kernel average misorientation (KAM) maps around the voids and intergranular cracks, as observed just beneath the fracture surface of the SSRT specimens with hydrogen charging temperature of 290K, 300K and 320K, respectively. The KAM value provides a qualitative measure of local crystal rotation and the resulting non-uniform plastic strain due to accumulated geometrically-necessary dislocations (GNDs) [72,73]. At a hydrogen charging temperature of 290K, some voids are generated from the interior of grains, as shown in Fig. 11. The nucleation of voids can be interpreted as a consequence of dislocation activities and plastic deformation, since these voids are accompanied by localised strain as seen in Fig. 11(c) and (d). Due to low diffusible hydrogen content (i.e., 3.7 wt ppm), only a few hydrogen atoms are segregated at the GBs, and there is a rather weak hydrogen interaction with lattice dislocations and the GBs. As such, the intergranular fracture cannot be observed at 290K. By contrast, Fig. 12 shows an intergranular brittle-like cracking at a hydrogen charging temperature of 300K. As a reflection of the substantial KAM values, highly localised strain is formed adjacent to the cracked GB area in Fig. 12(c) and (d). This suggests that the accumulation of lattice dislocations at GBs becomes significant at 300K, which is

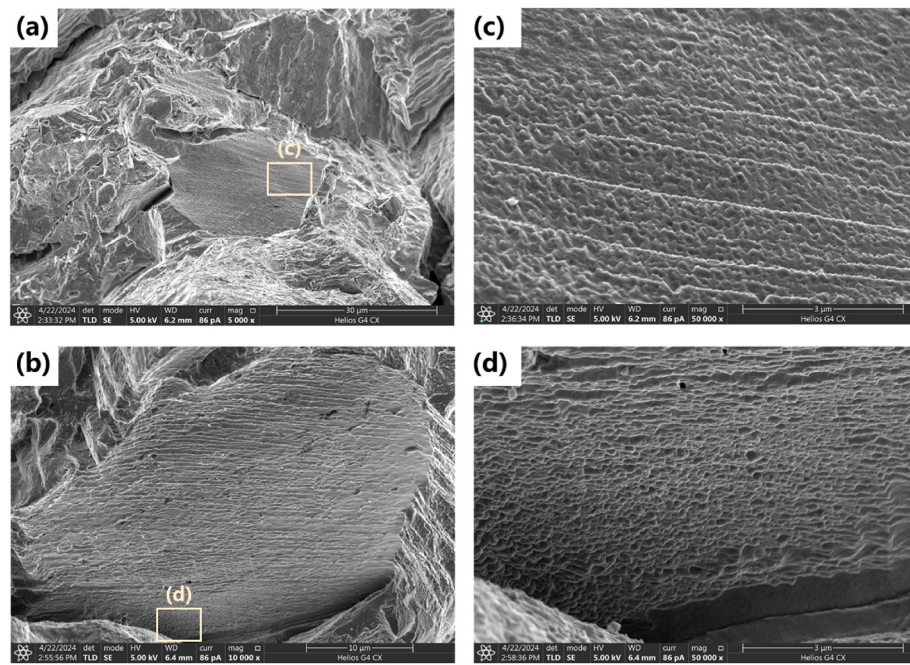


Fig. 10. SEM images of intergranular facets on the hydrogen-charged specimens at 300 K: (a) and (b) overview of intergranular facets, and (c) and (d) magnified view of marked region in (a) and (b), respectively.

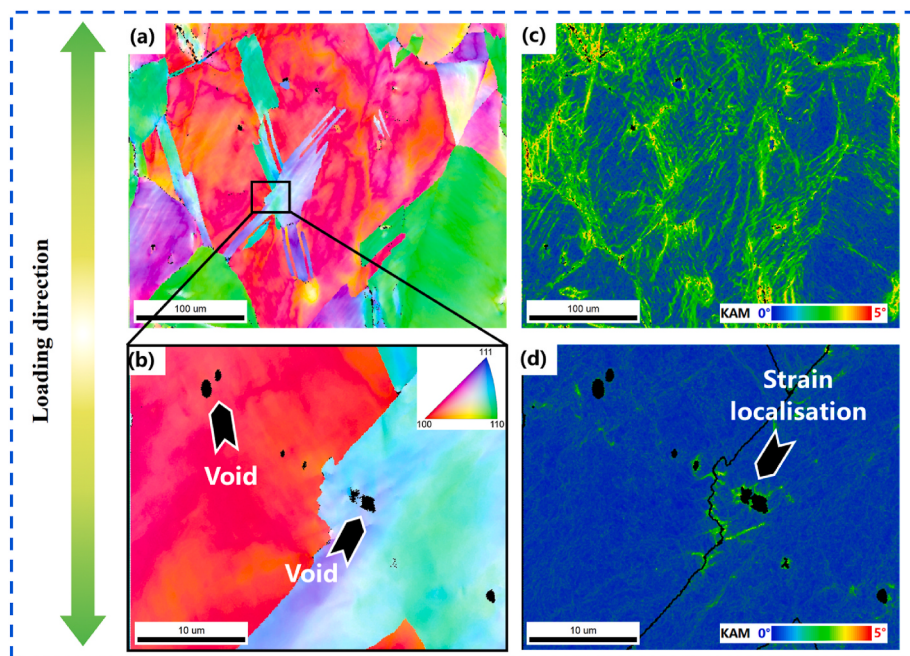


Fig. 11. Voids formed in the hydrogen-charged specimens at a charging temperature of 290 K, as analysed by EBSD. (a) and (b) are the crystallographic orientation maps with respect to the loading direction, and (c) and (d) are the corresponding KAM maps.

likely the precursor for the hydrogen-induced brittle cracking. Keep in mind that diffusible hydrogen content is the highest at $T_{HE, max}$ based on the TDS analysis, and a large number of hydrogen atoms are segregated at lattice sites, dislocations, and GBs. Moreover, dislocations can be capable of transporting diffusible hydrogen atoms along slip bands to the GBs under tensile deformation [24,74,75], encouraging the interaction between hydrogen and dislocations at the GBs and thus accumulating hydrogen atoms at the GB areas. Our previous atomistic calculations have revealed that hydrogen-dislocation-GB interactions can establish a boundary disruption and strain concentration, which

significantly reduces the theoretical cohesive strength and relaxed fracture energy of twenty types of hydrogen segregated GBs with $\langle 100 \rangle$, $\langle 110 \rangle$ and $\langle 111 \rangle$ tilt axis in Ni [69]. This potentially aggravates the nucleation of nano-voids and crack propagation along the GBs, leading to the ultimate intergranular fracture as schematically elaborated in Fig. 13.

Other researchers have also invoked the concept of hydrogen-dislocation-GB interactions in the hydrogen-induced cracking [12, 76–79]. For instance, Lu et al. [12] reported that in the presence of hydrogen, the GBs with higher resistance to slip transmission were more

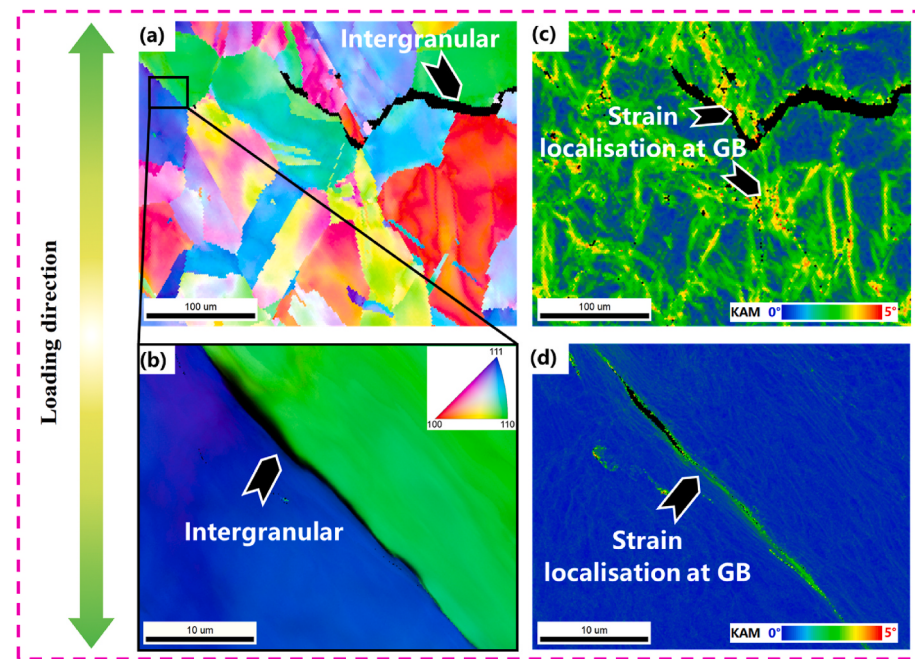


Fig. 12. Intergranular cracks formed in the hydrogen-charged specimens at a charging temperature of 300K, as analysed by EBSD. (a) and (b) are the crystallographic orientation maps with respect to the loading direction, and (c) and (d) are the corresponding KAM maps.

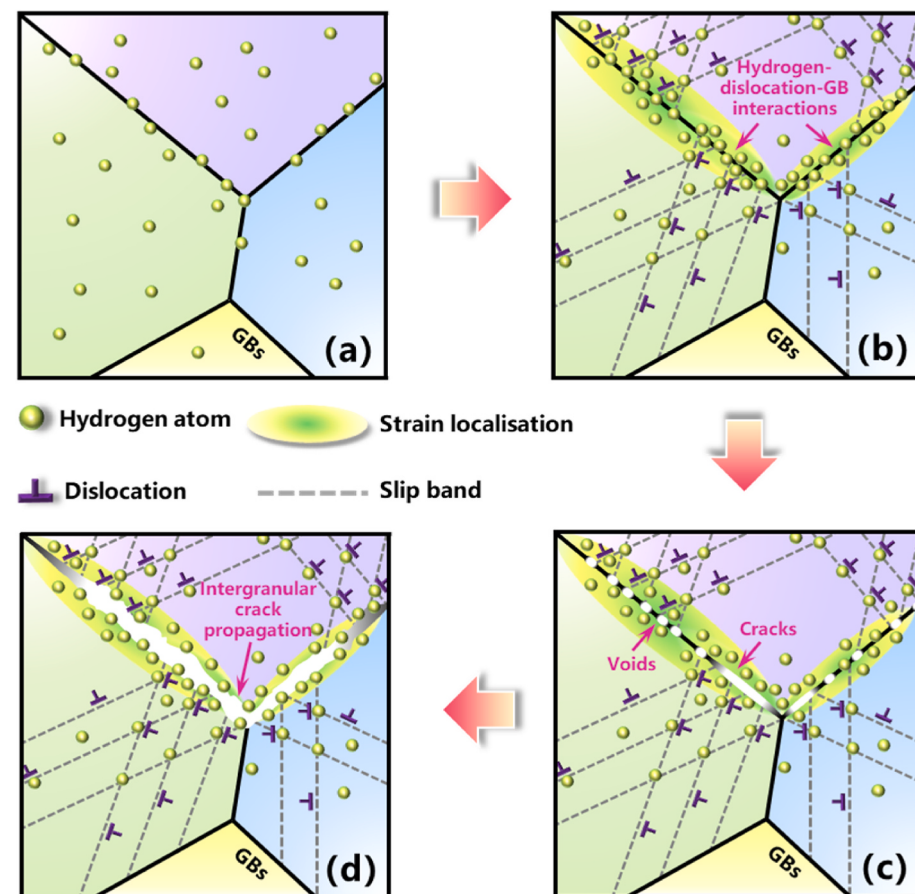


Fig. 13. Schematic illustrations of the envisaged mechanisms for hydrogen-induced intergranular crack propagation at a charging temperature of 300K: (a) diffusible hydrogen atoms at interstitial sites and GBs; (b) hydrogen transportation by dislocations and strain localisation as a consequence of hydrogen-dislocation-GB interactions; (c) void formation and crack initiation at the strain-concentrated GB area; (d) ultimate intergranular fracture due to crack propagation along GBs.

susceptible to crack initiation, which might be associated with hydrogen-enhanced dislocation activity and plasticity localisation at these boundaries. The interactions between dislocations and GBs were promoted by the presence of hydrogen, contributing to the formation of fine dimples, strain localisation and intergranular cracking. These arguments are consistent with our findings in Figs. 10 and 12. Nevertheless, one still needs to be reminded that, it is less likely that any single mechanism for HE is exclusively responsible for all hydrogen induced embrittlement process. There are experimental observations that twin boundaries can also facilitate hydrogen-induced cracking in Ni-based superalloys [80], Fe–Ni–Cr-based austenitic alloys [81] and high-Mn twinning-induced plasticity (TWIP) steel [82]. For such cases, it is likely that dislocation-twin interaction or twin-GB interaction can cause local stress concentration after severe strain. The hydrogen atoms present in the interaction sites can greatly facilitate the ultimate fracture [83], as can be envisioned as a generalization of the hydrogen-dislocation-GB interactions described here.

When the charging temperature further increases to 320K, there are also substantial KAM values and pronounced strain localisation adjacent to the GB area in Fig. 14(c). However, voids are directly nucleated from the interior of grains and the GBs as shown in Fig. 14(a) and (b), and there is no evidence of subsequent intergranular cracking, unlike the case of 300K. This discrepancy is primarily due to that the strain localisation in Fig. 14 is not a consequence of hydrogen-dislocation-GB interactions as mentioned above. At higher temperature hydrogen diffusion rate is faster [46,66,84], but the ability of dislocations in trapping and transporting hydrogen atoms along slip bands to the GBs is suppressed [22,24]. Furthermore, diffusible hydrogen content in the specimens at a hydrogen charging temperature of 320K is rather low (i.e., 5.8 wt ppm). These ingredients together limit hydrogen effects on dislocation plasticity and strain localisation nearby the GBs. On the other hand, previous literature reported that elevated temperature reduced unstable stacking fault energy, and thus enhanced dislocation plasticity for many types of materials such as iron [85], silicon [86], magnesium [87], chromium [88], and so on. As such, the observation of localised strain adjacent to the GB area is primarily ascribed to higher temperature, rather than hydrogen. It was revealed that strain localisation on its own was not the root cause for hydrogen-induced cracking

[15]. In addition, low diffusible hydrogen content and weak hydrogen trapping ability of GBs at higher temperature [89,90] cause a few hydrogen atoms to segregate at GBs. Such low hydrogen content at the GBs does not favour the crack initiation and propagation along the GBs.

From the above discussion, it can be concluded that hydrogen induced degradation reaches a maximum at 300K, below or above which the deterioration is less. At temperatures below or above 300 K, the failure process is characterised by a ductile fracture with void nucleation and growth within the grains. At 300 K, the fracture mode is intergranular brittle-like, which is associated with high diffusible hydrogen content and localised strain caused by hydrogen-dislocation-GB interactions.

5. Conclusions

The influence of temperature on hydrogen-induced embrittlement and corrosion behaviour of Ni-based superalloy 600 under electrochemical environment was systematically investigated through SSRT and potentiodynamic polarization experiments, in combination with detailed electron microscopy analysis. Furthermore, the underlying mechanisms behind $T_{HE, max}$ were demystified from the perspectives of hydrogen content and hydrogen-induced intergranular cracking. The central conclusions are identified as follows.

- With increasing the temperature, the final OCP value of the material in sulfuric acid shifts in the negative direction, and the anodic polarization branch exhibits a significant positive shift, rendering the aggravation of electrochemical corrosion process. Correspondingly, the corrosion morphology changes from pitting corrosion to intergranular corrosion.
- The material exhibits hydrogen-induced loss in ductility such as elongation to failure and reduction in area for all hydrogen charging temperatures of 280K–330K. The degree of degradation and HE index are the most markedly at a temperature of 300K. This indicates that the temperature threshold of $T_{HE, max}$ corresponds to 300K, and the HE susceptibility is less above and below $T_{HE, max}$.
- The fracture surfaces of the test specimens manifest with intergranular brittle fracture, secondary cracks at $T_{HE, max}$. The sufficiently

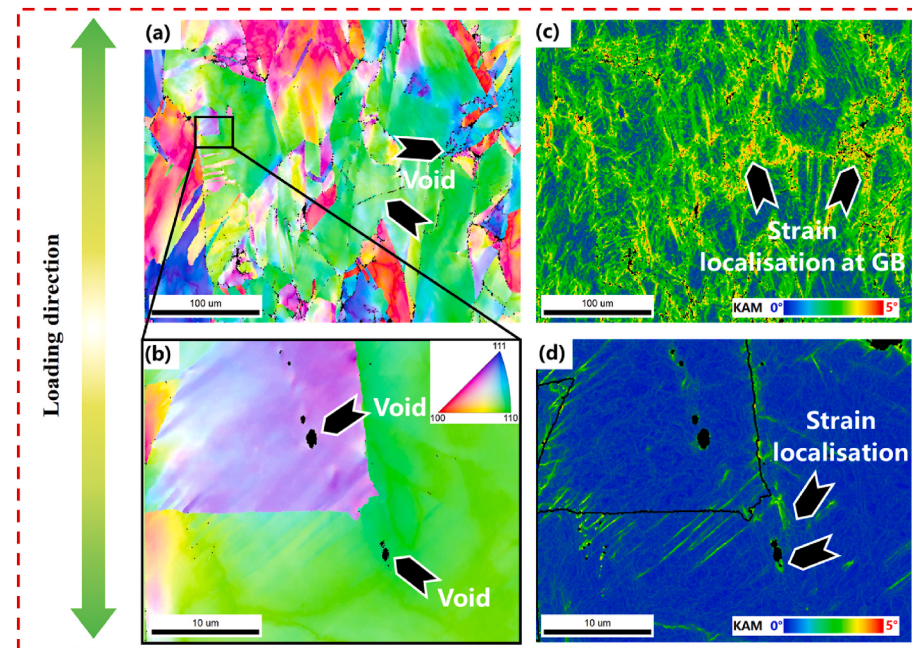


Fig. 14. Voids formed in the hydrogen-charged specimens at a charging temperature of 320K, as analysed by EBSD. (a) and (b) are the crystallographic orientation maps with respect to the loading direction, and (c) and (d) are the corresponding KAM maps.

high diffusible hydrogen content measured by TDS and highly localised strain adjacent to the cracked GB area characterized by EBSD point towards the underlying hydrogen-dislocation-GB interactions, which is the main contributor to the hydrogen-induced intergranular cracking at $T_{HE, max}$.

Data availability

The supporting data of this study are available from the corresponding author upon reasonable request.

Declaration of competing interest

The authors declare that they have no known competing financial interests or personal relationships that could have appeared to influence the work reported in this paper.

Acknowledgements

This study was financially supported by Early Career Researcher Grant (2024ECRG130) from The University of Melbourne, National Natural Science Foundation of China (No. 52205145), Nature Science Foundation of Fujian Province (No. 2023J05114), Talent Program of Fuzhou University (No. XRC-22024), and Qingyuan Innovation Laboratory Testing Fund of Precious Apparatus (No. QYT2023035).

Appendix A. Supplementary data

Supplementary data to this article can be found online at <https://doi.org/10.1016/j.jmrt.2025.03.043>.

References

- [1] Yue M, Lambert H, Pahon E, Roche R, Jemei S, Hissel D. Hydrogen energy systems: a critical review of technologies, applications, trends and challenges. *Renew Sustain Energy Rev* 2021;146:111180.
- [2] Kumar S, Arzaghi E, Baalsampang T, Garaniya V, Abbassi R. Insights into decision-making for offshore green hydrogen infrastructure developments. *Process Saf Environ Prot* 2023;174:805–17.
- [3] Rosen MA, Koohi-Fayegh S. The prospects for hydrogen as an energy carrier: an overview of hydrogen energy and hydrogen energy systems. *Energy Ecol Environ*. 2016;1:10–29.
- [4] Nicita A, Maggio G, Andaloro APF, Squadrito G. Green hydrogen as feedstock: financial analysis of a photovoltaic-powered electrolysis plant. *Int J Hydrogen Energy* 2020;45:11395–408.
- [5] Perez TE. Corrosion in the oil and gas industry: an increasing challenge for materials. *JOM* 2013;65:1033–42.
- [6] Furrer D, Fecht H. Ni-based superalloys for turbine discs. *JOM* 1999;51:14–7.
- [7] Stein-Brzozowska G, Flórez DM, Maier J, Scheffknecht G. Nickel-base superalloys for ultra-supercritical coal-fired power plants: fireside corrosion. Laboratory studies and power plant exposures. *Fuel* 2013;108:521–33.
- [8] Liu P, Wu Y, Zhong X, Wang Z, Oyama K, Ogota S, Watanabe Y, Shoji T. Quantitatively evaluating the contribution of intergranular carbides, Cr-depleted zone, and grain boundary to intergranular stress corrosion cracking of Alloy 600 in a simulated boiling water reactors environment with high oxygen concentrations. *Acta Mater* 2024;269:119794.
- [9] Ding Y, Yu H, Lin M, Ortiz M, Xiao S, He J, Zhang Z. Hydrogen trapping and diffusion in polycrystalline nickel: the spectrum of grain boundary segregation. *J Mater Sci Technol* 2024;173:225–36.
- [10] Chêne J, Brass AM. Role of temperature and strain rate on the hydrogen-induced intergranular rupture in alloy 600. *Metal Mater Trans A* 2004;35:457–64.
- [11] Ogawa Y, Takakuwa O, Okazaki S, Okita K, Funakoshi Y, Matsunaga H, Matsuoka S. Pronounced transition of crack initiation and propagation modes in the hydrogen-related failure of a Ni-based superalloy 718 under internal and external hydrogen conditions. *Corros Sci* 2019;161:108186.
- [12] Lu X, Wang D. Effect of hydrogen on deformation behavior of Alloy 725 revealed by in-situ bi-crystalline micropillar compression test. *J Mater Sci Technol* 2021;67: 243–53.
- [13] Takakuwa O, Ogawa Y, Yamabe J, Matsunaga H. Hydrogen-induced ductility loss of precipitation-strengthened Fe-Ni-Cr-based superalloy. *Mater Sci Eng, A* 2019; 739:335–42.
- [14] Ogawa Y, Noguchi K, Takakuwa O. Criteria for hydrogen-assisted crack initiation in Ni-based superalloy 718. *Acta Mater* 2022;229:117789.
- [15] Zhang Z, Obasi G, Morana R, Preuss M. Hydrogen assisted crack initiation and propagation in a nickel-based superalloy. *Acta Mater* 2016;113:272–83.
- [16] Qin L, Zhao M, Li Z, Rong L. Role of precipitates-decorated Σ3 twin boundaries on hydrogen-induced crack initiation and propagation in Ni-based superalloy 718. *Corros Sci* 2023;218:111189.
- [17] Li X, Zhang J, Akiyama E, Fu Q, Li Q. Hydrogen embrittlement behavior of Inconel 718 alloy at room temperature. *J Mater Sci Technol* 2019;35(4):499–502.
- [18] Li X, Yin J, Zhang J, Wang Y, Song X, Zhang Y, Ren X. Hydrogen embrittlement and failure mechanisms of multi-principal element alloys: a review. *J Mater Sci Technol* 2022;122:20–32.
- [19] Zhang Z, Moore KL, McMahon G, Morana R, Preuss M. On the role of precipitates in hydrogen trapping and hydrogen embrittlement of a nickel-based superalloy. *Corros Sci* 2019;146:58–69.
- [20] Lu X, Ma Y, Wang D. On the hydrogen embrittlement behavior of nickel-based alloys: alloys 718 and 725. *Mater Sci Eng, A* 2020;792:139785.
- [21] Michler T, Naumann J, Balogh MP. Hydrogen environment embrittlement of solution treated Fe–Cr–Ni super alloys. *Mater Sci Eng, A* 2014;607:71–80.
- [22] Murakami K, Yabe N, Suzuki H, Takai K, Hagihara Y, Wada Y. Substitution of high-pressure charge by electrolysis charge and hydrogen environment embrittlement susceptibilities for Inconel 625 and SUS 316L. In: ASME pressure vessels and piping conference; 2006. p. 563.
- [23] Lecoester JCF, Noel D. Hydrogen embrittlement of the Ni-base Alloy 600 correlated with hydrogen transport by dislocations. *Mater Sci Eng, A* 1999;262:173–83.
- [24] Michler T, Schweizer F, Wackermann K. Review on the influence of temperature upon hydrogen effects in structural alloys. *Metals* 2021;11:423.
- [25] Liu Y, Wu Y, Yu J, Ju J, Zhang Z, Kang M, Wang J, Sun B, Ning Y. Temperature-dependent deformation mechanisms and microstructural degradation of a polycrystalline nickel-based superalloy. *J Alloys Compd* 2019;775:181–92.
- [26] Lee W-J, Lee J-Y, Oh S-K, Yang H, Park J, Baek UB, Lee Y-K. Temperature dependency of hydrogen embrittlement resistance of austenitic Fe–24Mn–3Cr–0.5Cu–0.47C steel. *Mater Sci Eng, A* 2024;889:145838.
- [27] Chêne J, Brass AM. Role of temperature and strain rate on the hydrogen-induced intergranular rupture in alloy 600. *Metall Mater Trans A* 2004;35:457–64.
- [28] Noguchi K, Ogawa Y, Takakuwa O, Matsunaga H. Internal and external hydrogen-related loss of ductility in a Ni-based superalloy 718 and its temperature dependence. *Tetsu to Hagane* 2021;107:59–71.
- [29] Kritzer P. Corrosion in high-temperature and supercritical water and aqueous solutions: a review. *J Supercrit Fluids* 2004;29:1–29.
- [30] Hwang SS, Kim HP, Lee DH, Kim UC, Kim JS. The mode of stress corrosion cracking in Ni-base alloys in high temperature water containing lead. *J Nucl Mater* 1999; 275:28–36.
- [31] Yamazaki S, Lu Z, Ito Y, Takeda Y, Shoji T. The effect of prior deformation on stress corrosion cracking growth rates of Alloy 600 materials in a simulated pressurized water reactor primary water. *Corros Sci* 2008;50:835–46.
- [32] Kang Y, Leng X, Zhao L, Bai B, Wang X, Chen H. Review on the corrosion behaviour of nickel-based alloys in supercritical carbon dioxide under high temperature and pressure. *Crystals* 2023;13(5):725.
- [33] Lortakul P, Trice RW, Trumble KP, Dayananda MA. Investigation of the mechanisms of Type-II hot corrosion of superalloy CMSX-4. *Corros Sci* 2014;80: 408–15.
- [34] Brooking L, Gray S, Sumner J, Nicholls JR, Marchant G, Simms NJ. Effect of stress state and simultaneous hot corrosion on the crack propagation and fatigue life of single crystal superalloy CMSX-4. *Int J Fatig* 2018;116:106–17.
- [35] Zhang Y, Knowles D, Withers PJ. Microstructural development in Pt-aluminide coating on CMSX-4 superalloy during TMF. *Surf Coat Technol* 1998;107:76–83.
- [36] Brooking L, Sumner J, Gray S, Simms NJ. Stress corrosion of Ni-based superalloys. *Mater A T High Temp* 2017;35:120–9.
- [37] Yamazaki S, Lu Z, Ito Y, Takeda Y, Shoji T. The effect of prior deformation on stress corrosion cracking growth rates of Alloy 600 materials in a simulated pressurized water reactor primary water. *Corros Sci* 2008;50:835–46.
- [38] Lu J, Xu Z, Geng T, Xu Z. Temperature dependence of electrochemical characteristics on the growth surface and isomorphous perpendicular surface of DD6. *Electrochim Acta* 2024;486:144121.
- [39] Lv X, Jiang Q, Zhang J, Zhang J, Huang Z, Duan J, Hou B. Electrochemical behaviors of Ni-base superalloy CMSX-4 in 3.5 wt.% NaCl: effect of temperature and preoxidation. *Materials* 2020;13(23):5478.
- [40] Sun H, Wu X, Han EH. Effects of temperature on the protective property, structure and composition of the oxide film on Alloy 625. *Corros Sci* 2009;51(11):2565–72.
- [41] Luo H, Sohn SS, Lu W, Li L, Li X, Soundararajan CK, Krieger W, Li Z, Raabe D. A strong and ductile medium-entropy alloy resists hydrogen embrittlement and corrosion. *Nat Commun* 2020;11:3081.
- [42] Lu X, Wang D, Johnsen R. Hydrogen diffusion and trapping in nickel-based alloy 625: an electrochemical permeation study. *Electrochim Acta* 2022;421.
- [43] Li J, Wu Z, Zhu L, Zhang Z, Teng L, Zhang L, Lu C, Wang R, Zhang C. Investigations of temperature effects on hydrogen diffusion and hydrogen embrittlement of X80 pipeline steel under electrochemical hydrogen charging environment. *Corros Sci* 2023;223:111460.
- [44] Long H, Mao S, Liu Y, Zhang Z, Han X. Microstructural and compositional design of Ni-based single crystalline superalloys—A review. *J Alloys Compd* 2018;743: 203–20.
- [45] Kou H, Li W, Ma J, Shao J, Tao Y, Zhang X, Geng P, Deng Y, Li Y, Zhang X. Theoretical prediction of the temperature-dependent yield strength of solid solution strengthening Nickel-based alloys. *Int J Mech Sci* 2018;140:83–92.
- [46] Xu J, Hao Z, Fu Z, He X, Wang H, Xu G. Hydrogen embrittlement behavior of selective laser-melted Inconel 718 alloy. *J Mater Res Technol* 2023;23:359–69.
- [47] Holbrook J, West A. The effect of temperature and strain rate on the tensile properties of hydrogen-charged 304 L, 21-6-9 and JBK 75, hydrogen eff. *Met*. 1980; 655–63.

- [48] Quadrini E. The effect of temperature on hydrogen induced fracture in UNI 40NiCrM07 steel. *Mater Chem Phys* 1988;20:73–85.
- [49] Clark WG. Effect of temperature and pressure on hydrogen cracking in high strength type 4340 steel. *J Mater Energy Syst* 1979;1:33–40.
- [50] Platt P, Sayers J, Horner DA, Barrow A, Engelberg DL. Hydrogen-induced brittle fracture in nickel based alloy 82 weld metal. *Corros Sci* 2019;153:118–26.
- [51] Hakiki N, Boudin S, Rondot B, Belo MDC. The electronic structure of passive films formed on stainless steels. *Corros Sci* 1995;37:1809–22.
- [52] Tomashov N, Altovsky R, Chernova G. Passivity and corrosion resistance of titanium and its alloys. *J Electrochem Soc* 1961;108:113.
- [53] Tomcsanyi L, Varga K, Bartik I, Horányi H, Maleczki E. Electrochemical study of the pitting corrosion of aluminium and its alloys—II. Study of the interaction of chloride ions with a passive film on aluminium and initiation of pitting corrosion. *Electrochim Acta* 1989;34:855–9.
- [54] Wu T-F, Cheng T-P, Tsai W-T. The electrochemical potentiokinetic reactivation behavior of Alloy 600. *Mater Chem Phys* 2001;70:208–16.
- [55] Ahn MK, Kwon HS, Lee JH. Predicting susceptibility of alloy 600 to intergranular stress corrosion cracking using a modified electrochemical potentiokinetic reactivation test. *Corrosion* 1995;51:441–9. Medium: X; Size.
- [56] Cardoso M, Amaral S, Martini E. Temperature effect in the corrosion resistance of Ni–Fe–Cr alloy in chloride medium. *Corros Sci* 2008;50:2429–36.
- [57] Carranza R, Alvarez M. The effect of temperature on the passive film properties and pitting behaviour of a FeCrNi alloy. *Corros Sci* 1996;38:909–25.
- [58] Gildenpfennig G, Gramberg U, Hohlneicher G. Passivation and corrosion of the metallic high performance materials Alloy 33 and MC-Alloy in different environments. *Corros Sci* 2003;45:575–95.
- [59] Harrington DA, Conway B. Ac Impedance of Faradaic reactions involving electrocatalyzed intermediates—I. Kinetic theory. *Electrochim Acta* 1987;32: 1703–12.
- [60] Krstajić N, Popović M, Grgur B, Vojnović M, Šepa D. On the kinetics of the hydrogen evolution reaction on nickel in alkaline solution: Part I. The mechanism. *J Electroanal Chem* 2001;512:16–26.
- [61] Zheng Y, Jiao Y, Jaroniec M, Qiao SZ. Advancing the electrochemistry of the hydrogen-evolution reaction through combining experiment and theory. *Angew Chem Int Ed* 2015;54:52–65.
- [62] Tian X, Zhao P, Sheng W. Hydrogen evolution and oxidation: mechanistic studies and material advances. *Adv Mater* 2019;31:1808066.
- [63] Daftt E, Bohnenkamp K, Engell H. Investigations of the hydrogen evolution kinetics and hydrogen absorption by iron electrodes during cathodic polarization. *Corros Sci* 1979;19:591–612.
- [64] Schmidt T, Ross Jr P, Markovic N. Temperature dependent surface electrochemistry on Pt single crystals in alkaline electrolytes: Part 2. The hydrogen evolution/oxidation reaction. *J Electroanal Chem* 2002;524:252–60.
- [65] Clouser S, Huang J, Yeager E. Temperature dependence of the Tafel slope for oxygen reduction on platinum in concentrated phosphoric acid. *J Appl Electrochem* 1993;23:597–605.
- [66] Xing X, Pang Z, Zhang H, Liu J, Cui G. Study of temperature effect on hydrogen embrittlement in X70 pipeline steel. *Corros Sci* 2024;230.
- [67] Claeyns L, Cnockaert V, Depover T, De Grawe I, Verbeeken K. Critical assessment of the evaluation of thermal desorption spectroscopy data for duplex stainless steels: a combined experimental and numerical approach. *Acta Mater* 2020;186:190–8.
- [68] Li W, Wu W, Yang Z, Liu M, Li S, Li J. Enhancement of hydrogen embrittlement resistance in 310S austenitic stainless steel through ribbon-like δ-ferrite. *Corros Sci* 2024;233.
- [69] Li J, Lu C, Pei L, Zhang C, Wang R. Atomistic investigation of hydrogen induced decohesion of Ni grain boundaries. *Mech Mater* 2020;150:103586.
- [70] Li J, Lu C, Pei L, Zhang C, Tieu K. Influence of solute hydrogen on the interaction of screw dislocations with vicinal twin boundaries in nickel. *Scripta Mater* 2019;173: 115–9.
- [71] Angelo JE, Moody NR, Baskes MI. Trapping of hydrogen to lattice defects in nickel. *Model Simulat Mater Sci Eng* 1995;3:289.
- [72] An X, Zhang H, Zhang D, Zhu J, Wang Q, Zhu T, Shi Y, Cao X, Deng H, Hu W, Yang T. Mechanisms of hydrogen embrittlement resistances in FCC concentrated solid solution alloys. *Corros Sci* 2024;229.
- [73] Mao LY, Luo ZA, Huang C, Zhou HY, Zhang XM. Exploring the hydrogen embrittlement behavior in nickel-economized austenitic stainless steel: investigating the role of manganese in modifying hydrogen-induced crack mechanisms. *Corros Sci* 2024;226.
- [74] Dadfarnia M, Martin ML, Nagao A, Sofronis P, Robertson IM. Modeling hydrogen transport by dislocations. *J Mech Phys Solid* 2015;78:511–25.
- [75] Tien J, Thompson AW, Bernstein IM, Richards RJ. Hydrogen transport by dislocations. *Metall Trans A* 1976;7:821–9.
- [76] Wan L, Geng WT, Ishii A, Du J-P, Mei Q, Ishikawa N, Kimizuka H, Ogata S. Hydrogen embrittlement controlled by reaction of dislocation with grain boundary in alpha-iron. *Int J Plast* 2019;112:206–19.
- [77] Wang S, Martin ML, Sofronis P, Ohnuki S, Hashimoto N, Robertson IM. Hydrogen-induced intergranular failure of iron. *Acta Mater* 2014;69:275–82.
- [78] Martin ML, Dadfarnia M, Nagao A, Wang S, Sofronis P. Enumeration of the hydrogen-enhanced localized plasticity mechanism for hydrogen embrittlement in structural materials. *Acta Mater* 2019;165:734–50.
- [79] Martin M, Somerday B, Ritchie R, Sofronis P, Robertson I. Hydrogen-induced intergranular failure in nickel revisited. *Acta Mater* 2012;60:2739–45.
- [80] Seita M, Hanson J, Gradečák S, Demkowicz M. The dual role of coherent twin boundaries in hydrogen embrittlement. *Nat Commun* 2015;6:6164.
- [81] Chen S, Zhao M, Rong L. Hydrogen-induced cracking behavior of twin boundary in γ phase strengthened Fe–Ni based austenitic alloys. *Mater Sci Eng, A* 2013;561: 7–12.
- [82] Koyama M, Akiyama E, Tsuzaki K, Raabe D. Hydrogen-assisted failure in a twinning-induced plasticity steel studied under in situ hydrogen charging by electron channeling contrast imaging. *Acta Mater* 2013;61:4607–18.
- [83] Li J, Lu C, Pei L, Zhang C, Tieu K. Influence of solute hydrogen on the interaction of screw dislocations with vicinal twin boundaries in nickel. *Scr Mater* 2019;173: 115–9.
- [84] Xing X, Cheng R, Cui G, Liu J, Gou J, Yang C, Li Z, Yang F. Quantification of the temperature threshold of hydrogen embrittlement in X90 pipeline steel. *Mater Sci Eng, A* 2021;800.
- [85] El Ters P, Shehadeh MA. On the strain rate sensitivity of size-dependent plasticity in BCC iron at elevated temperatures: discrete dislocation dynamics investigation. *Mech Mater* 2020;148:103494.
- [86] Schaffar GJ, Tscharnauer D, Maier-Kiener V. Exploring the high-temperature deformation behavior of monocrystalline silicon—An advanced nanoindentation study. *Mater Des* 2023;233:112198.
- [87] Saito K, Uchiyama Y, Sato K, Kimura M, Ishida H, Hiraga K. High-temperature plastic-deformation behavior of Mg–(Y/Zn) supersaturated solid-solution alloys and the resulting dislocation structures. *Mater Trans* 2020;61:647–56.
- [88] Choi I-C, Brandl C, Schwaiger R. Thermally activated dislocation plasticity in body-centered cubic chromium studied by high-temperature nanoindentation. *Acta Mater* 2017;140:107–15.
- [89] Galliano F, Andrieu E, Blanc C, Cloue J-M, Commetable D, Odemer G. Effect of trapping and temperature on the hydrogen embrittlement susceptibility of alloy 718. *Mater Sci Eng, A* 2014;611:370–82.
- [90] Sanchez J, Ridruejo A, de Andres PL. Diffusion and trapping of hydrogen in carbon steel at different temperatures. *Theor Appl Fract Mech* 2020;110:102803.